Research on Engineering Structures & Materials

www.jresm.org

Research Group

Research Article

Enhancing photovoltaic pumping systems through machine learning–based modeling and optimization

Islam Hachemi [*,1,a], Kamel Haddouche [1,b], Ahmed Bouzidane [1,c], Mustapha Belarbi [2,d]

[1]*Research Laboratory of Industrial Technologies, Faculty of Applied Sciences, University of Tiaret, B. P. 78 Zaâroura 14000 Tiaret, Algeria*

[2]*Energy Engineering and Computer Engineering Laboratory, Faculty of Applied Sciences, University of Tiaret, B. P. 78 Zaâroura 14000 Tiaret, Algeria*

Article Info

Article History:

Received 27 Oct 2025

Accepted 20 Feb 2026

Keywords:

Machine learning; modeling; PV pumping system; Simulation; Identification; Optimization

Abstract

This paper deals with the enhancement of photovoltaic water pumping systems through machine learning–based modeling and optimization. First, parameter identification of the target PV module KC200GT is carried out using three algorithms: Newton–Raphson, fsolve, and particle swarm optimization (PSO). Among these methods, PSO shows the best agreement with the manufacturer's data, achieving best performance (R2 = 0.9901 and RMSE = 0.0358). In addition, manufacturer data of the centrifugal pump, generally given for a unique nominal speed, are used to develop a model capable of predicting the pump flow rate, total head, and load torque at different rotational speeds. Furthermore, four machine-learning models - artificial neural networks (ANN), adaptive neuro-fuzzy inference system (ANFIS), support vector machine (SVM), and Gaussian process regression (GPR) - are evaluated for predicting the maximum power point voltage. Comparative analysis indicates that ANFIS achieves the highest prediction accuracy, followed by GPR, ANN, and SVM, outperforming conventional algorithms. Consequently, ANFIS combined with a PI regulator is adopted as the control strategy for tracking the maximum power point. Finally, the dynamic behavior of the photovoltaic water pumping system is examined under variations in irradiance and temperature. The results demonstrate that the proposed control strategy effectively maintains the PV voltage close to its optimal value and responds rapidly to changing climatic conditions, confirming its suitability for PV water pumping applications.

1. Introduction

A photovoltaic water pumping system (PVWPS) is a self-sustained system powered by only solar energy. The lack of drinking and irrigation water was always a problem, especially in isolated locations. For this purpose, PVWPS offers an effective solution by supplying water whenever sufficient sunlight is available. Moreover, by incorporating storage tanks, this system can ensure a continuous water supply and meet demand even during nighttime or low-sunlight periods.

The effectiveness of the PV array in the PVWPS may be affected by changes in climate conditions and pumping load. These challenges can be addressed using maximum power point tracking (MPPT) techniques, which can extract the maximum power from the PV generator. Among these techniques, the conventional methods perturb and observe (P&O) and incremental conductance (INC) are the most widely used due to their simplicity.

*Corresponding author: hachemi.islam1414@gmail.com

[a]orcid.org/0009-0001-5487-0648; [b]orcid.org/0000-0002-7084-0246; [c]orcid.org/0009-0001-9731-1870; [d]orcid.org/0000-0002-0614-9944

DOI: http://dx.doi.org/10.17515/resm2026-1303en1027rs

In recent years, artificial intelligence (AI)-based methods have been increasingly utilized across various research areas and industries to enhance services and address challenges that traditional methods cannot solve. These methods can be utilized to tackle the challenges of MPPT. Haddad et al. [1] presented several ANN-based methods for predicting water flow rates in a PVWPS. Their findings demonstrated accurate predictions based on measured temperature and irradiance. In [2], the authors present a Matlab-implemented SVM model for predicting photovoltaic energy production using irradiance and ambient temperature as inputs. Similarly, another method involving SVM is presented in [3]. A multi-input SVM model was evaluated using three input combinations: solar power alone, solar power with solar irradiance, and solar power with temperature and irradiance. In another work, the authors in [4] propose a SVM–based MPPT approach to estimate the maximum power point (MPP) of a PV panel using irradiance and temperature inputs. The estimated MPP voltage is then used to compute the duty cycle of the boost converter. Simulation results demonstrate effective MPP tracking with an efficiency exceeding 94%.

Chandra et al. [5] have introduced a novel photovoltaic power system topology incorporating an RBF neural network to enhance system efficiency. It is demonstrated that this MPPT method delivers greater efficiency than the conventional techniques. In [6], the authors present an ANN methodology for MPPT applied to a symmetrical multilevel boost converter in a solar-powered system. This innovative approach improves the output power under varying solar conditions. The results indicate enhanced efficiency by 99.99% and significant reductions in settling and rising times. The authors in [7] studied the impact of increasing the number of hidden layers in a neural network on predicting photovoltaic power. Several network structures were designed and trained using module temperature and solar radiation as inputs, and PV power as the output. Their results show that increasing the number of hidden layers significantly improves prediction accuracy. In [8], an ANFIS integrated with a proportional PI controller is presented for MPPT in a solar-powered brushless DC motor used for water pumping applications. Simulation studies conducted under Matlab confirm the controller's effectiveness, and experimental verification demonstrates its practicality. Sarkar et al. [9] introduced a novel hybrid model by integrating a Bat algorithm for training to enhance the ANFIS. The results demonstrate that this metaheuristic approach provides superior training efficiency in comparison with standard backpropagation. A hybrid method was proposed in [10] by employing the Crowded Plant Height Optimization algorithm for ANFIS training resulted in improved tracking speed and efficiency relative to the standard ANFIS model. Ahmed et al. [11] developed and implemented a soft-computing-based MPPT controller to predict the optimal converter duty cycle under varying climatic conditions and total static heads. A comparative study of the proposed soft-computing algorithms was conducted to evaluate and validate their accuracy. In [12], a hybrid FL-INC optimization algorithm is presented for PVWPS utilizing a SEPIC converter to enhance performance. This method combines fuzzy-logic with INC to maximize power extraction and improve PVWPS efficiency. In [13], the authors proposed a method utilizing a Genetic Algorithm (GA) to optimize gains for a backstepping controller (BSC) in MPPT for solar photovoltaic systems. This approach enhances tracking efficiency and stability, achieving MPP in 0.2 seconds, significantly outperforming conventional methods.

MPPT techniques based on ML techniques require significant real-time computation and therefore rely on powerful microcontrollers or DSPs. Integrating MPPT controllers with power system controllers (PSCs) requires careful coordination between power electronics, microcontrollers, and sensors to ensure stable and efficient operation under real-world conditions, such as changing irradiance and temperature [14]. Variations in solar irradiance caused by shading and clouds, along with the thermal degradation of PSCs, require fast and adaptive MPPT methods [15]. In practical conditions, sensors must remain accurate over a wide temperature range. In addition, real-world MPPT systems must be resistant to environmental factors such as dust and moisture.

This study investigates a PVWPS comprising a PV generator, DC/AC inverter, squirrel-cage induction motor, MPPT controller, centrifugal pump, and hydraulic circuit. Accurate modeling of such a system is essential for predicting behavior and optimizing control. A key aspect of this modeling involves the identification of critical components, such as the PV module. Where its parameters are identified using three methods: particle swarm optimization (PSO), Newton-

Raphson, and fsolve. In addition, the dynamic behavior of the entire PVWPS must be considered to develop an effective control strategy. To address these challenges, this study incorporates ML techniques such as ANN, ANFIS, SVM, and GPR for MPPT, with the goal of improving system adaptability under varying weather conditions. However, few studies combine parameter identification, ML-based MPPT, and dynamic modeling of the PVWPS within a unified framework. This work aims to fill that gap by providing a comprehensive evaluation to support the development of reliable and high-performance PVWPS. The remainder of the paper is organized into five sections. In section 2, the mathematical modeling of the various components of the PVWPS will be presented. In section 3, a comparative analysis between four ML models will be conducted. The simulation results are discussed in section 4. Furthermore, the parameters of the target PV module and centrifugal pump are presented. The last section summarizes the results of this work and concludes.

2. PVWPS Modeling

The investigated PVWPS is composed of different elements: PV generator, DC/AC inverter, squirrel-cage induction motor, MPPT controller, centrifugal pump, and hydraulic circuit including the pipes and storage tank. **Hata! Başvuru kaynağı bulunamadı.** depicts a simplified illustration of the overall studied system.

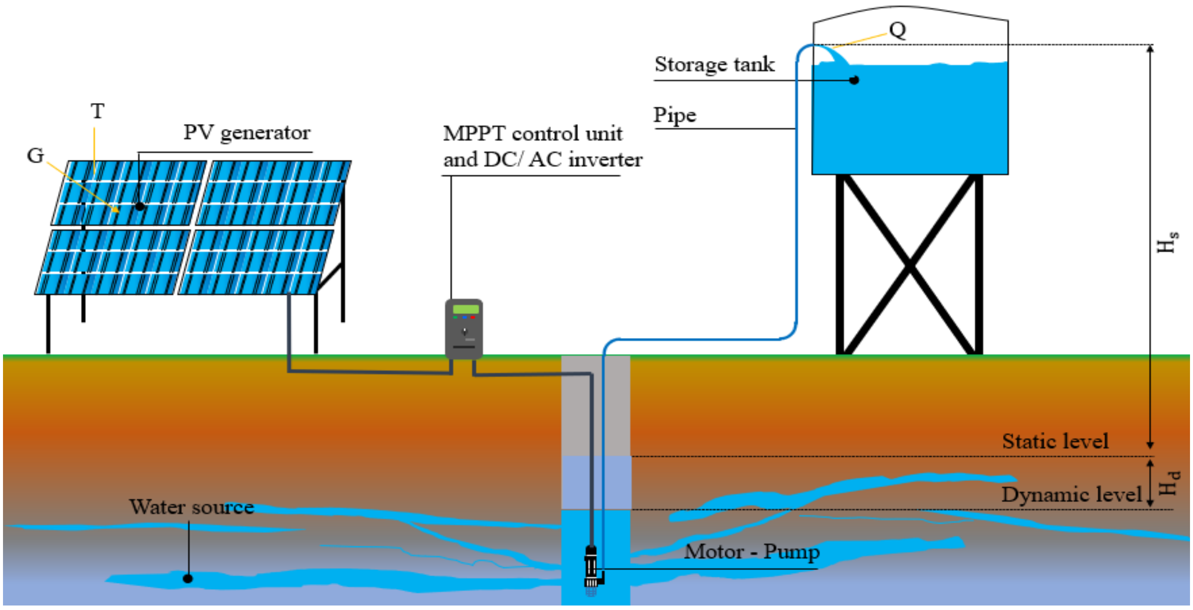

Fig. 1. Schematic of PV water pumping system

2.1. PV Generator

The PV generator is a group of modules connected in series/parallel to obtain the desired power. The basic element in a PV module is the solar cell; there are several mathematical models that describe its behavior [16]. This work employs the one-diode model, where the output current of a solar cell is described by:

$$I = \frac{G}{G_{ref}}\left(I_{ph\_ref} + \mu_{sc}\cdot\left(T_c - T_{c\_ref}\right)\right) - I_0\cdot\left(e^{\frac{q\cdot(V+R_S\cdot I)}{A\cdot k\cdot T_C}} - 1\right) - \left(\frac{V + R_s\cdot I}{R_{sh}}\right) \tag{1}$$

where, G: Solar irradiance intensity, G_{ref}: Solar irradiance intensity at STC, I_{ph_ref}: Photocurrent at STC, T_{c_ref}: Cell temperature at STC, T_c: Cell temperature, μ_{sc}: Coefficient temperature of short circuit current (A/K), I_0: Reverse saturation current of the diode, q: Electron charge, R_{sh}: PV module's shunt resistance, R_s: PV module's series resistance, k: Boltzmann constant, A: Diode ideality factor.

While the single-diode model is simpler with five unknown parameters (R_s, R_{sh}, A, I_0, I_{ph}), it may not capture the complexities of the PV cell's behavior as accurately as the double-diode model, particularly under diverse operating conditions; its simplicity, efficiency, and sufficient accuracy make it suitable for many processes optimization and system design applications.

Irradiance absorbed by the solar cell leads to a continuous increase in temperature and a growing temperature gradient between the solar cell and the environment. This temperature differential drives an escalation in the rate of heat dissipation by the solar cell. At some point, an equilibrium state is reached where the rate of heat loss matches the rate of solar energy absorption; thus, the following equation is obtained:

$$\varepsilon \cdot S \cdot G = h \cdot S \cdot (T_c - T_{amb}) \tag{2}$$

Solving the last equation, T_c is expressed by the following equation:

$$T_c = T_{amb} + \frac{\varepsilon}{h} \cdot G = T_{amb} + \alpha \cdot G \tag{3}$$

The parameter (α) can be obtained through interpolation of the measured data; however, it is commonly accepted to be equal to 0.03 [17]. This value corresponds to a temperature increase of 30 K for a flux of 1000 W/m^2.

The generator is composed of multiple PV modules interconnected in series and/or parallel configurations to obtain specific voltage and current requirements. The overall output current and voltage of the generator can be determined as follows:

$$\begin{cases} I_{gen} = N_p \cdot I \\ V_{gen} = N_s \cdot V \end{cases} \tag{4}$$

2.2. DC/AC Inverter

The main function of the DC/AC inverter is to transform the DC voltage produced by the solar generator into a three-phase voltage with variable frequency. The output voltages of a three-phase inverter can be computed by the following equation:

$$\begin{bmatrix} V_a \\ V_b \\ V_c \end{bmatrix} = \frac{V_{dc}}{3} \begin{bmatrix} 2 & -1 & -1 \\ -1 & 2 & -1 \\ -1 & -1 & 2 \end{bmatrix} \cdot \begin{bmatrix} S_1 \\ S_2 \\ S_3 \end{bmatrix} \tag{5}$$

With S_i is the state of the switch (IGBT), Si = 0 if it is open and Si = 1 if it is closed.

2.3. Squirrel-Cage Induction Motor

The voltage of the three-phase squirrel-cage induction motor can be computed in a d-q frame by the following equation [18]:

$$\begin{aligned} \begin{bmatrix} V_{ds} \\ V_{qs} \end{bmatrix} &= R_s \begin{bmatrix} I_{ds} \\ I_{qs} \end{bmatrix} + \frac{d}{dt} \begin{bmatrix} \varphi_{ds} \\ \varphi_{qs} \end{bmatrix} + \omega_s \begin{bmatrix} 1 & 0 \\ 0 & 1 \end{bmatrix} \begin{bmatrix} \varphi_{ds} \\ \varphi_{qs} \end{bmatrix} \\ \begin{bmatrix} V_{dr} \\ V_{qr} \end{bmatrix} &= R_r \begin{bmatrix} I_{dr} \\ I_{qr} \end{bmatrix} + \frac{d}{dt} \begin{bmatrix} \varphi_{dr} \\ \varphi_{qr} \end{bmatrix} + \omega_r \begin{bmatrix} 1 & 0 \\ 0 & 1 \end{bmatrix} \begin{bmatrix} \varphi_{dr} \\ \varphi_{qr} \end{bmatrix} \end{aligned} \tag{6}$$

For the d-axis, V_{ds}, I_{ds}, φ_{ds}, V_{dr}, I_{dr} and φ_{dr} referred to stator and rotor voltage, current, and flux linkage, respectively. For the q-axis, the last variables are referred V_{qs}, I_{qs}, φ_{qs}, V_{dr}, I_{dr} and φ_{dr}. R_s and R_r are stator and rotor winding resistance. ω_s and ω_r are stotor and rotor frequency. For this study, V_{dr} and I_{dr} are set to zero. The currents of the asynchronous motor in the d-q frame are given as follows:

$$\begin{bmatrix} I_{ds} \\ I_{qs} \end{bmatrix} = \frac{L_r}{L_s \cdot L_r - M_{sr}^2} \begin{bmatrix} \varphi_{ds} \\ \varphi_{qs} \end{bmatrix} - \frac{M_{sr}^2}{L_s \cdot L_r - M_{sr}^2} \begin{bmatrix} \varphi_{dr} \\ \varphi_{qr} \end{bmatrix}$$
$$\begin{bmatrix} I_{dr} \\ I_{qr} \end{bmatrix} = \frac{L_r}{L_s \cdot L_r - M_{sr}^2} \begin{bmatrix} \varphi_{dr} \\ \varphi_{qr} \end{bmatrix} - \frac{M_{sr}^2}{L_s \cdot L_r - M_{sr}^2} \begin{bmatrix} \varphi_{ds} \\ \varphi_{qs} \end{bmatrix} \tag{7}$$

where, L_s: Stator inductance, , L_r: Rotor inductance, M_{sr}: Mutual inductance. The electromagnetic torque of the motor can be computed as follows [19]:

$$T_{em} = 1.5 \cdot p \cdot \left(\varphi_{ds} \cdot I_{qs} - \varphi_{qs} \cdot I_{ds}\right) \tag{8}$$

where, p: Pair pole number. The motor speed is calculated using the mechanical dynamic equation:

$$T_{em} = \frac{J}{p}\frac{d\omega_r}{dt} + f\omega_r + T_r \tag{9}$$

where, T_r: Load torque, f: Viscous torque constant, J: Inertia moment of the rotor.

2.4 Pump and Hydraulic Circuit

The hydraulic power needed to pump water at a volumetric rate (Q) and total head (H) is given by the following equation:

$$P_h = g \cdot \rho \cdot H \cdot Q \tag{10}$$

The pump efficiency (η) is given by the following equation:

$$\eta = \frac{P_h}{\omega_r \cdot T_r} \tag{11}$$

The load torque can be expressed as follows:

$$T_r = \frac{g \cdot \rho \cdot H \cdot Q}{\omega_r \cdot \eta} \tag{12}$$

In general, pumps are described by their H(Q) characteristic that defines the total head as a function of flow rate for a single nominal speed (N_n); the equation that links the total head with the flow rate for any rotational speed (N) is given as follows:

$$H(Q, N^*) = h_0 \cdot (N^*)^2 - h_1 \cdot N^* \cdot Q - h_2 \cdot Q^2 \tag{13}$$

where, $N^* = \frac{N}{N_n}$: Normalized speed. The load torque caused by flow through the hydraulic part of the pump takes a similar form to the total head equation, and can be written as:

$$T_r(Q, N^*) = c_0 \cdot (N^*)^2 - c_1 \cdot N^* \cdot Q - c_2 \cdot Q^2 \tag{14}$$

The coefficients h_0, h_1, h_2, c_0, c_1 and c_2 are calculated from the data provided by the manufacturer.

The mathematical formulation governing the hydraulic circuit is provided below. The pump must work against the total head, which includes static head H_s, dynamic head H_d, and total head loss in the pipe. The total head is done by the following equation:

$$HMT = H_s + H_d + \left(\lambda \cdot \frac{L}{d} + K\right)\frac{8Q^2}{g\pi^2 d^4} \tag{15}$$

where, λ: Friction factor, K: Total fitting loss coefficient.

The head loss in pipe due to frictional effects can be determined from the Darcy-Weisbach equation. For laminar flow, λ is equal to 64/Re. For turbulent flow of incompressible fluids, this factor can be determined from the Moody diagram. To avoid the reading error, λ is determined from the Colebrook equation.

2.5 Maximum Power Point Tracking (MPPT)

To enhance the energy efficiency of PV systems, it is essential to design an effective MPPT technique. Traditionally, the MPP has been tracked using conventional algorithms such as P&O and INC. The P&O method is widely used due to its simplicity; it works by slightly perturbing the operating voltage and observing changes in output power to approach the MPP. The INC algorithm is based on the slope of the power-voltage (P–V) curve, which equals zero at the MPP. While these classical techniques are effective under steady conditions, their performance often degrades under rapidly changing environmental conditions such as partial shading or sudden irradiance variations. To address these limitations, recent research has turned to Machine Learning (ML) techniques. By integrating AI into MPPT strategies, PV systems can achieve faster convergence, improved accuracy, and better adaptability, making these techniques a promising direction for future advancements in solar energy technologies. For this purpose, a comparative analysis of ML techniques will be conducted in this study.

3. Comparative Analysis of ML Techniques

This section presents a comparative analysis of ML techniques applied to predict the optimal voltage used as a reference signal of the PI controller. The observed data are derived through a numerical compilation based on measurements provided by the manufacturer. The mathematical formulations of ML techniques are reported in Appendix A.

The dataset is segregated into two subsets: training and testing; 70% of the dataset is used for the training, while the remainder is utilized for the testing phase. In addition, the following considerations are adopted:

- ANN structure: A feedforward network is considered with three layers: an input layer, a hidden layer, and an output layer. The inputs, for each ML model, are the irradiance and temperature; the output is the MPP voltage. The ANN structure is 2-x-1. The number of hidden neurons (x) is taken equal to “3”; this value is selected via different simulations to maximize R and to minimize MSE. For activation or transfer functions, layers 2 and 3 are concerned. A linear activation function for the output (layer 3) and a hyperbolic tangent sigmoid one for the single hidden layer (layer 2) are selected. In addition, Bayesian Regularization is opted as a training algorithm.
- Regarding ANFIS, a Sugeno FIS is adopted with a “4 3” structure by using the “Neuro-Fuzzy Designer” application under MATLAB. A Gaussian membership function is taken for the inputs, and a constant one for the output. In addition, a grid partition and hybrid learning method are considered during simulation limited to a maximum of 30 epochs. Notice that different types of membership functions (triangular …) are tested, and we selected the one that offers the best predictions (Gaussian).
- The SVM model is trained using a quadratic kernel function. MATLAB provides six kernel functions (linear, quadratic, cubic, fine-Gaussian, medium-Gaussian, and coarse-Gaussian). After several simulations, the quadratic kernel yielded the best performance, with default following hyper-parameters: Box-constraint “auto mode”, Epsilon “auto mode”, Kernel-scale “auto mode”, Standardize “yes”.
- The selected GPR technique employed a Matern 5/2 kernel function. This last is selected from a range of tested kernels, including Rational Quadratic, Squared Exponential, and Exponential. Default settings are adopted under MATLAB for the hyper-parameters.

The training of these techniques is performed offline based on weather conditions. During simulation, the ML-MPPT receives the input information and provides predictions instantaneously, which is analogous to a testing phase. The simulation outcomes obtained during the training and testing phases using ANN, ANFIS, SVM, and GPR are presented in Table 1.

Table 1. Comparison between the observed and predicted values of V_{MPP}

Data	Inputs		Observed	Predicted V_{MPP} (V)			
	T (°C)	G (kW/m²)	V_{MPP} (V)	ANN	ANFIS	SVM	GPR
Training	20	1	382.34	381.69	382.06	385.98	381.99
	20	0.6	414.54	416.28	414.53	413.91	415.67
	20	0.4	428.40	427.52	429.03	424.74	427.95
	25	1	368.48	369.37	369.27	371.89	369.11
	25	0.8	386.96	386.29	386.47	386.77	386.58
	25	0.4	414.54	413.68	414.05	410.27	413.52
	25	0.2	419.16	418.20	418.63	418.89	418.41
	30	0.8	373.10	371.92	372.47	372.63	372.41
	30	0.6	386.96	387.89	388.06	385.30	387.57
	30	0.2	400.68	402.96	400.93	404.36	402.40
	35	1	340.90	341.48	340.86	343.94	341.04
	35	0.6	373.10	372.31	372.04	371.11	372.32
	35	0.4	382.34	382.93	382.77	381.55	382.82
	40	1	327.04	326.86	326.66	330.08	326.49
	40	0.8	340.90	341.42	341.82	344.58	341.93
	40	0.4	368.48	367.49	368.22	367.31	367.99
	40	0.2	373.10	372.25	373.14	375.54	372.70
	50	0.8	313.18	312.66	313.15	316.84	313.14
	50	0.6	327.04	328.21	327.21	328.99	327.79
	50	0.4	340.90	340.02	340.39	339.06	339.80
	50	0.2	345.38	346.12	345.73	347.03	345.88
Testing	20	0.8	400.68	399.36	398.84	400.99	399.65
	20	0.2	433.02	432.34	434.88	433.49	433.82
	25	0.6	400.68	402.74	402.15	399.57	402.16
	30	1	354.62	355.82	354.98	357.88	355.39
	30	0.4	396.06	398.59	397.53	395.87	398.16
	35	0.8	354.62	356.75	357.22	358.57	357.33
	35	0.2	386.96	387.37	386.85	389.91	387.05
	40	0.6	354.62	356.73	355.90	356.99	356.94
	50	1	299.32	298.88	298.14	302.60	299.13

To evaluate the performance of predictive models, RMSE, R-squared, and MAPE between observed and predicted values are used; their expressions are given as follows:

$$RMSE = \sqrt{\frac{\sum_{k=1}^{n}\left(V_{MPP\,obs}(k) - V_{MPP\,pred}(k)\right)^2}{n}} \tag{16}$$

$$R^2 = 1 - \frac{\sum_{k=1}^{n}\left(V_{MPPobs}(k) - V_{MPPpred}(k)\right)^2}{\sum_{k=1}^{n}\left(V_{MPPobs}(k) - \bar{V}_{MPPobs}(k)\right)^2} \tag{17}$$

$$MAPE\ (\%) = 100 \times \frac{1}{n}\sum_{k=1}^{n}\frac{\left|V_{MPP\,obs}(k) - V_{MPP\,pred}(k)\right|}{V_{MPP\,obs}(k)} \tag{18}$$

Table 2 presents a comparative analysis of the performance indicators for the ML models. The results reveal that all models exhibit strong performance, characterized by high R-squared (0.9935–0.9997), low RMSE (0.5472–2.5902), and low MAPE (0.1194 %–0.6143 %). Notably, the ANFIS model demonstrates high accuracy during both training and testing, followed by GPR and ANN. The SVM model, although exhibiting reasonable performance during both training and testing. Considering the results across all data points, the ANFIS demonstrates superior predictive accuracy with the lowest overall RMSE and MAPE, and a higher R-squared.

Table 2. Performance indicators for the ML models

		ANN	ANFIS	SVM	GPR
Training data	RMSE	0.9971	0.5472	2.5902	0.7613
	R-Squared	0.9990	0.9997	0.9935	0.9994
	MAPE (%)	0.2386	0.1194	0.6143	0.1775
Testing data	RMSE	1.6206	1.5305	2.4242	1.5504
	R-Squared	0.9981	0.9983	0.9957	0.9982
	MAPE (%)	0.3808	0.3606	0.5633	0.3402
All data	RMSE	1.2181	0.9552	2.5415	1.0615
	R-Squared	0.9987	0.9992	0.9943	0.9990
	MAPE (%)	0.2813	0.1918	0.5990	0.2263

Under MATLAB environment, three validation schemes are available for the Regression Learner application. First, the ML models were compared using the resubstitution validation by considering 70%–30% training–testing split. About the overfitting risks, k-fold cross-validation (k = 3) and holdout validation were employed as additional assessments for the SVM and GPR models. Despite the difference in performance during the learning phase, the results obtained during the testing phase indicate consistent performance for both algorithms. The extended validation results for the SVM and GPR models are summarized in Table 3.

Table 3. Performance of SVM and GPR under different validation schemes

Phase	Validation scheme	SVM		GPR	
		RMSE	R-Squared	RMSE	R-Squared
Training	Resubstitution	2.5902	0.9935	0.7613	0.9994
	3-fold cross	5.1716	0.9754	3.563	0.983
	Holdout	3.9106	0.9907	3.3287	0.9933
Testing	Resubstitution	2.4204	0.9957	1.5504	0.9962
	3-fold cross	2.5636	0.9952	1.5504	0.9982
	Holdout	2.93	0.9897	1.2653	0.9981

Figs. 2-3 show the comparison between observed and predicted results for the training and testing phases. A comparison of the performances between the predictive models based on ML techniques and those using conventional algorithms is depicted in Fig. 4. Step changes in irradiance level were applied at 2 s and 3 s. Irradiance level is changed from 0.5 kW/m^2 to 0.640 kW/m^2, then from 0.640 kW/m^2 to 0.47 kW/m^2.

Fig. 4 indicates that the ML techniques exhibit superior prediction performance compared to other conventional methods, as evidenced by a faster rise time of 0.033 s in contrast to the 0.2 and 0.4 s rise times observed in INC and P&O methods, respectively. In addition, to simulate the PVWPS under realistic operating conditions and to assess the robustness of the control strategy, noise measurement is added to the input signals, with variances of 50 W/m^2 for irradiance and 0.04 °C for temperature. Based on the outcomes of this comparative analysis, ANFIS with a PI regulator is employed for performance enhancement of the system control strategy due to its higher accuracy compared to the other three ML based MPPT, as well as conventional P&O and INC methods.

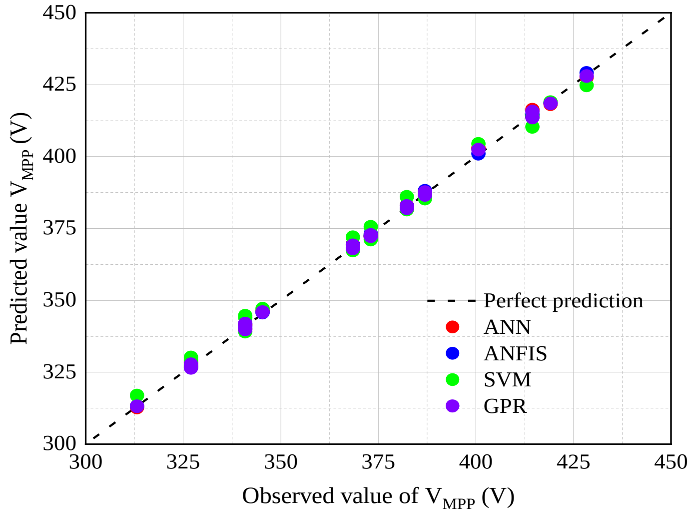

Fig. 1. Comparison between observed and predicted results for the training phase

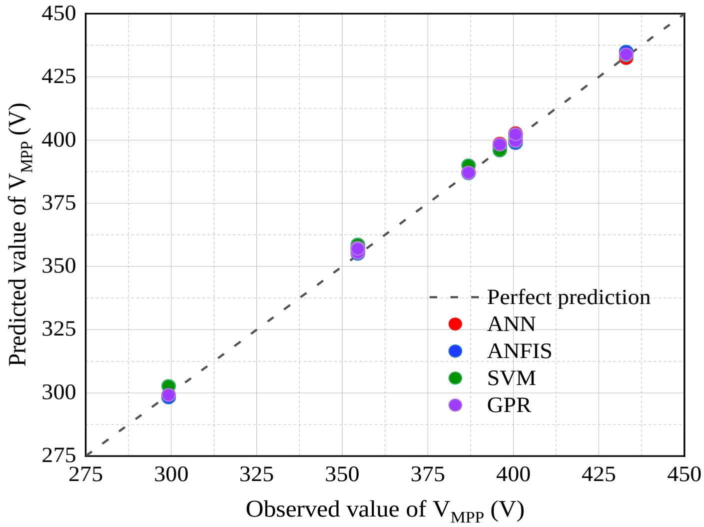

Fig. 2. Comparison between observed and predicted results for the testing phase

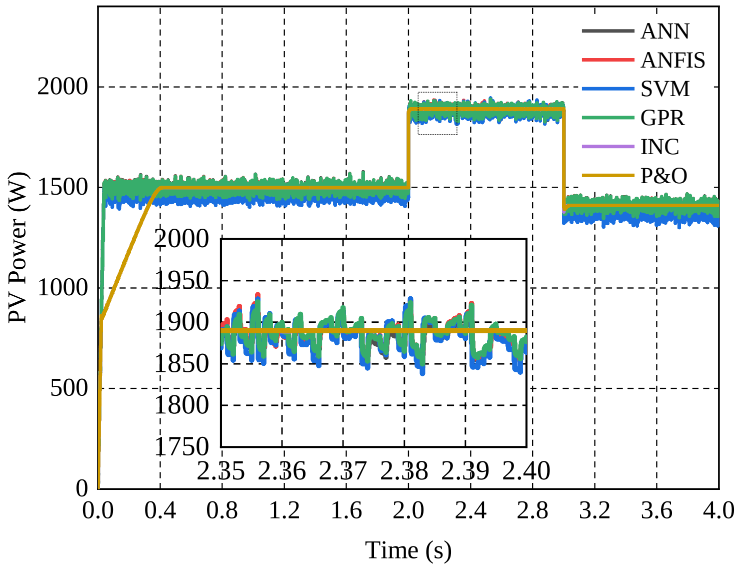

Fig. 3. PV power for a change in Irradiance levels

4. Results and Discussion

In this study, each component of the PVWPS has been programmed under the Matlab/Simulink environment. The system parameters used in the simulation are given in Appendix B. The pumping system has variable inputs, which are the weather conditions (solar irradiance and temperature), and has the flow rate as an output. The main objective is to find an operating point to manage the interactions between the solar irradiance, temperature, and flow rate. As can be seen from Fig. 5, the entire system model consists mainly of four interactive parts. The first part makes the connection between the voltage at the PV generator terminals and the current required by the inverter. The second part presents the link between the rotational speed of the squirrel cage motor and the load torque exerted by the pump on its shaft. The third part made the connection between the supply voltage at the inverter terminals and the current absorbed by the motor. The fourth connection is between the flow rate and the total head.

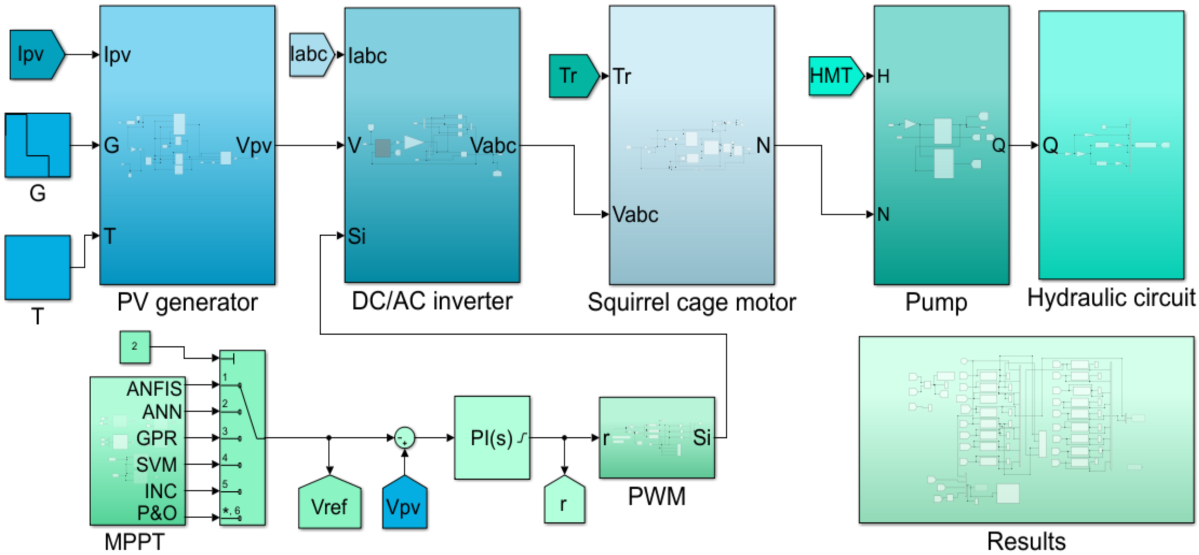

Fig. 4. Dynamic modeling of the PVWPS under Matlab/Simulink

The MPPT control strategy consists of two elements: the first one is the MPPT based on ANFIS, and the second element is the PI controller. The ANFIS uses actual irradiance and temperature to predict the optimal voltage used as a reference signal for the controller PI. The last adjusts the ratio (r = V/f) of the PWM. The parameters obtained for the PI controller are: proportional and integral gains (k_p = 0.25 and k_i = 0.542).

Compared to the previous study conducted in reference [18], the present work employs the KC200GT PV module. To this end, the parameters of the PV module were identified using three methods: Newton-Raphson, fsolve, and PSO. Table 4 summarizes the estimated parameters obtained using these different methods.

Table 4. Identified parameters for the KC200GT PV module

Parameter	Analytical method [20]	Lambert W function [20]	Ref. [21]	Newton-Raphson	fsolve	PSO
R_s (Ω)	0.308	0.284057	0.23	0.3144	0.31074	0.2349
R_{sh} (Ω)	193.049394	157.85322	113.997	186.7473	192.3	167.4838
A	1.075812	1.075816	1.06	1.06	1.07	1.1348
I_s (μA)	2.15236	2.19541	1.75	1.5440	1.9042	5.8094
I_{ph} (A)	8.2233	8.21	8. 193	8.2238	8.22327	8.18281

Regarding the accuracy of the results (see Table 5), the PSO method provides excellent agreement with the manufacturer's data with a lower RMSE of 0.0358 and a higher R^2 of 0.9901. In contrast, the Newton-Raphson and fsolve methods exhibit relatively higher RMSE values of 0.1195 and 0.1190, respectively; this demonstrates lower accuracy in the region of the MPP (see Fig. 6).

Additionally, comparisons with results reported in references [20] and [21] reveal notable deviations in the open-circuit voltage region and to the right of the MPP. The simulated I-V curves of the KC200GT PV module using parameters estimated by the three methods at T = 25 °C and G = 1000 W/m^2 are presented in Fig. 6.

Table 5. Performance indicators for the identification methods

	Analytical method [20]	Lambert W function [20]	Ref. [21]	Newton-Raphson	fsolve	PSO
RMSE	0.1189	0.1002	0.0858	0.1195	0.1190	0.0358
R-squared	0.8908	0.9224	0.9431	0.8896	0.8905	0.9901

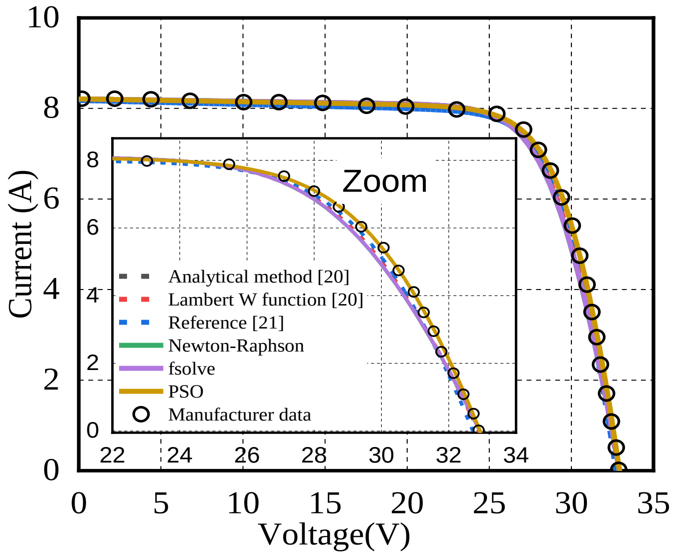

Fig. 5. I-V characteristic for the KC200GT PV module

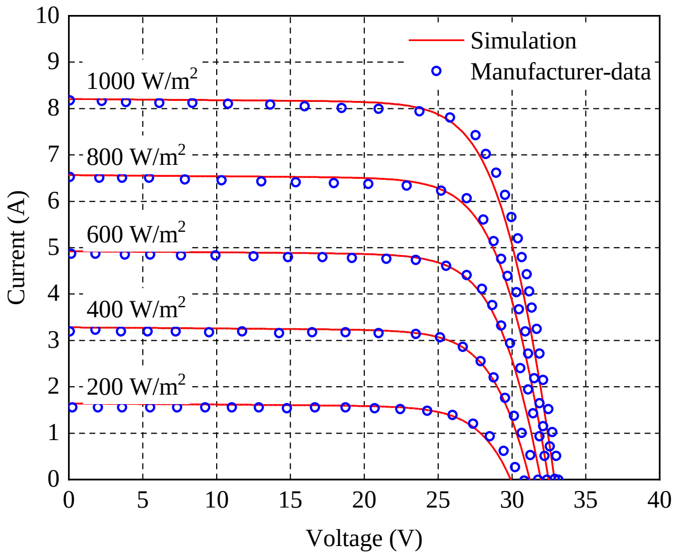

Fig. 6. I-V characteristic under different irradiances and constant temperature T = 25 °C

The I-V characteristics of the target PV module, provided by the manufacturer and simulation, are depicted in Fig. 7 with irradiance levels ranging from 200 W/m^2 to 1000 W/m^2 and constant temperature maintained at 25 °C. It can be seen that the modeling by the one-diode model of the solar cell gives a good agreement between the provided manufacturer data and simulated results.

Table 6. Coefficients for computing (H) and (T_r) for different rotational speeds

Coefficient	h_0	h_1	h_2	c_0	c_1	c_2
Value	74.9	3.559	-5.594	1.957	3.476	-0.6107

The second element of the PV pumping system, which has changed according to the previous work in [17] is the centrifugal pump. Notice that the pump manufacturer gives the H(Q) and η(Q) characteristics for a single nominal speed. For this last, it is possible to calculate the load torque by utilizing eq (12). Table C of Appendix C illustrates the manufacturer's data of the pump for a nominal rotational speed Nn = 2900 rpm; eq (13) and eq (14) are used to obtain (H) and (T_r) for different speeds. The characteristics H(Q, N) and T_r (Q, N) of the selected pump (Bombas Ideal VIP 9/6) are illustrated in Figs. 7–8, respectively. The coefficients reported in Table 6 are obtained with polynomial interpolation by using data reported in Appendix C.

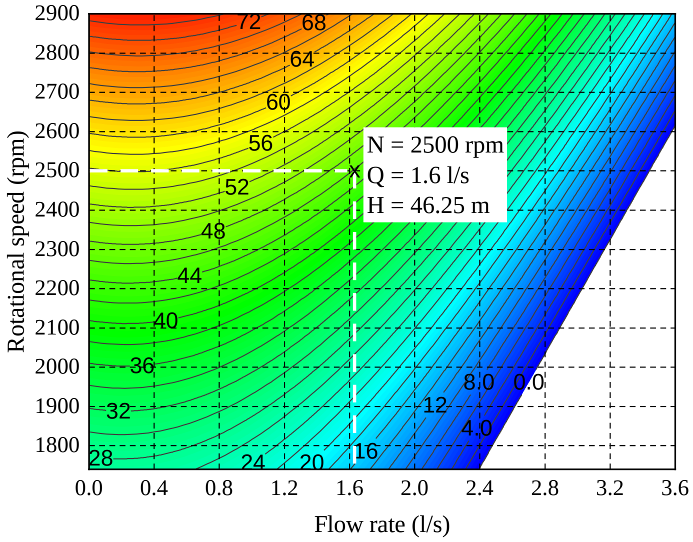

Fig. 8. Total head curves

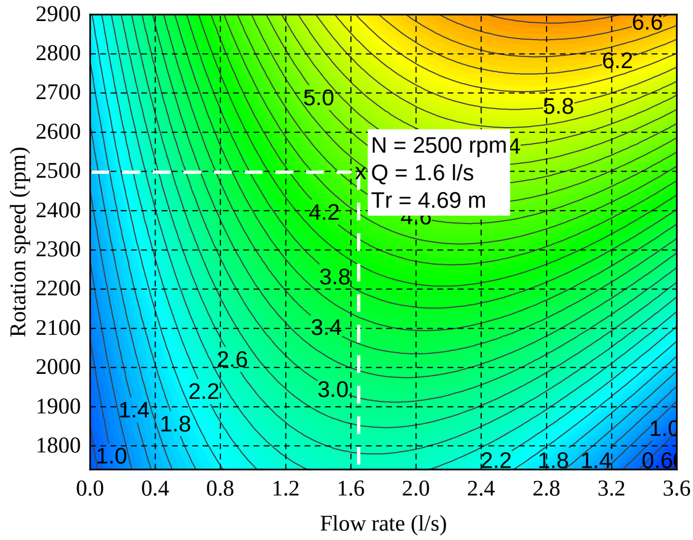

Fig. 9. Load torque curves

Fig. 8 and Fig. 9 show, for N = 2500 rpm and Q = 1.6 l/s, the obtained values of the total head H = 46.25 m and load torque Tr = 4.69 N·m, respectively. In the following, the simulation results of PVWPS for variations in irradiance and temperature will be presented.

4.1 Effect of Irradiance

The simulation was performed over a duration of 4 s. To evaluate the dynamic response of the MPPT, a step change in solar irradiance from 700 W/m² to 500 W/m² was applied at t = 2 s, while the operating temperature was maintained at 25 °C. The simulations depicted in Fig. 10 to Fig. 19 represent, respectively, the variations over time of voltage and current at PV generator terminals, PV power, line voltages and line currents at the motor terminals, rotational speed, electromagnetic and load torques, total head, water flow rate, and total head losses. Fig. 10 depicts the profile of the voltage at the PV generator terminals and the reference voltage predicted by ANFIS over time. It can be observed that the proposed control strategy has operated the photovoltaic generator near its optimal voltage, where it effectively adjusts to the irradiance change for a relatively short duration of 0.04 s. It is also noticeable a slight decrease in the optimal voltage during sunlight variations, attributed to the negligible impact of irradiance levels on Voc voltage. Consequently, the effect of irradiance change on V_{MPP} is deemed negligible as well. On the contrary, in Fig. 11, a significant impact on the current of the PV generator can be observed, with a decrease from 5 to 3.7 A; this reduction is accompanied by a decrease in generated power from 2048 W to 1498 W (Fig. 12); this is attributed to the notable effect of sunlight levels on the Isc current. According to Fig. 13, the transient regimes of the motor are relatively insignificant, where the current demand during the transient regime is approximately 1.5 times higher than that in the nominal regime.

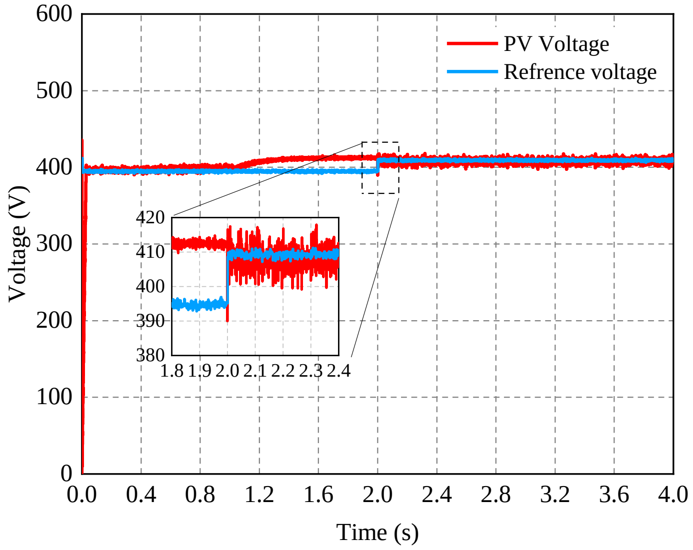

Fig. 10. PV voltage response to an irradiance drop (G: 700→500 W/m²)

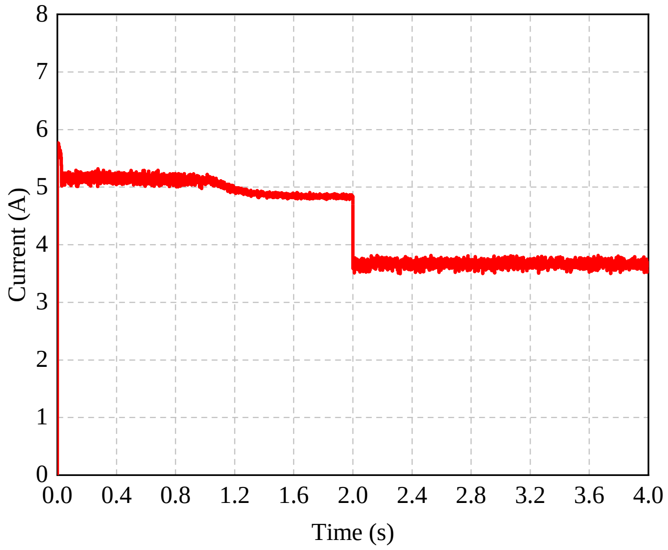

Fig. 11. PV current response to an irradiance drop (G: 700→500 W/m²)

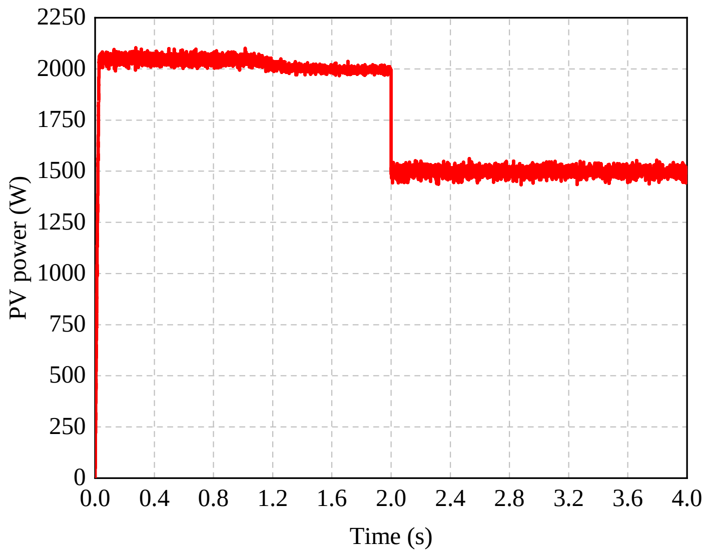

Fig. 12. PV power response to an irradiance drop (G: 700→500 W/m²)

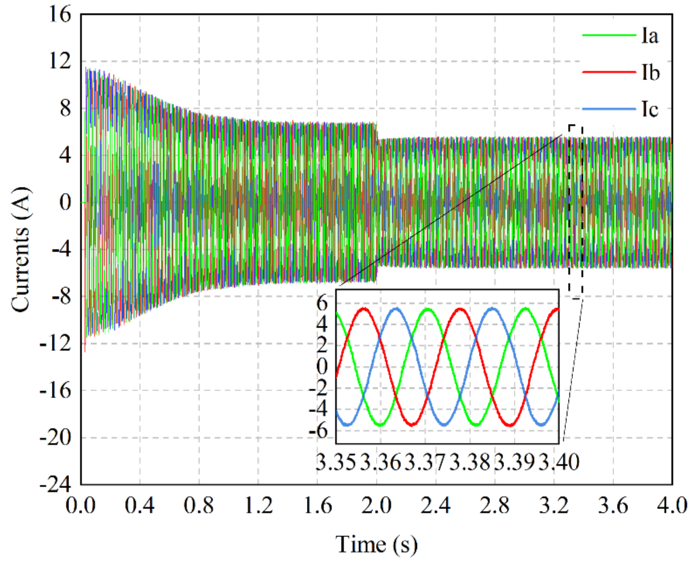

Fig. 13. Line current response to an irradiance drop (G: 700→500 W/m²)

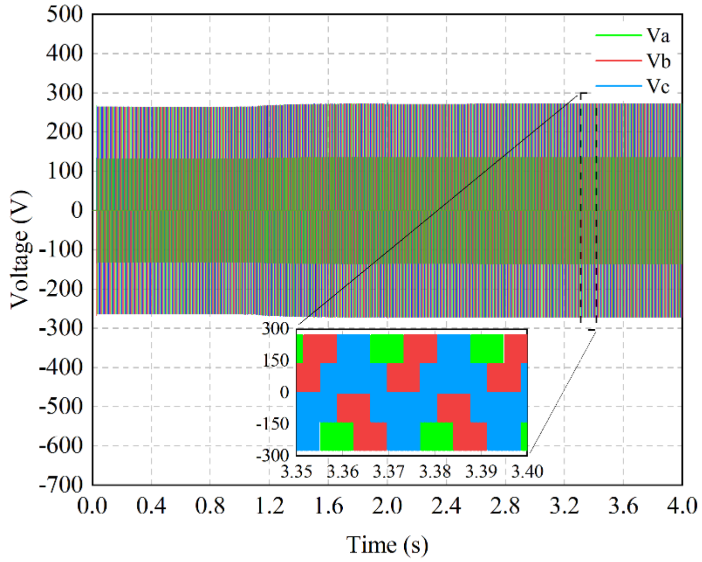

Fig. 14. Line voltages response to an irradiance drop (G: 700→500 W/m²)

The proposed control strategy enables a gradual start-up of the load to ensure a current demand lower than that of the short circuit of the PV generator. According to Fig. 14, the motor is supplied with voltages closer to the nominal values. Additionally, it can be observed that the voltage has increased by a small value of 13 V during the variation in irradiance. As shown in Fig. 16, the motor took 1.2 s for its rotational speed to reach the nominal speed. This period also corresponds to the transient oscillation phase of the electromagnetic torque, as depicted in Fig. 15. In addition, the decrease in electromagnetic torque and the rotational speed indicate that the system has shifted to another operating point to adapt the load to the available power. The variance between the electromagnetic torque and the resistive torque is due to the influence of viscous friction occurring within the motor.

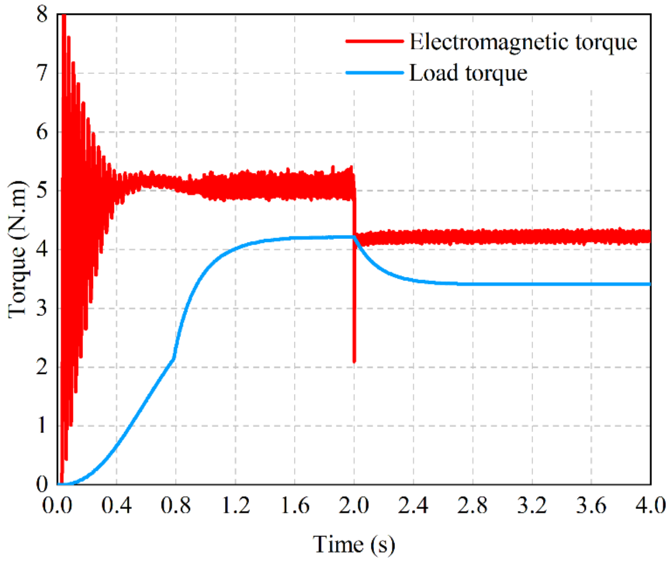

Fig. 15. Electromagnetic and load torque responses to an irradiance drop (G: 700→500 W/m^2)

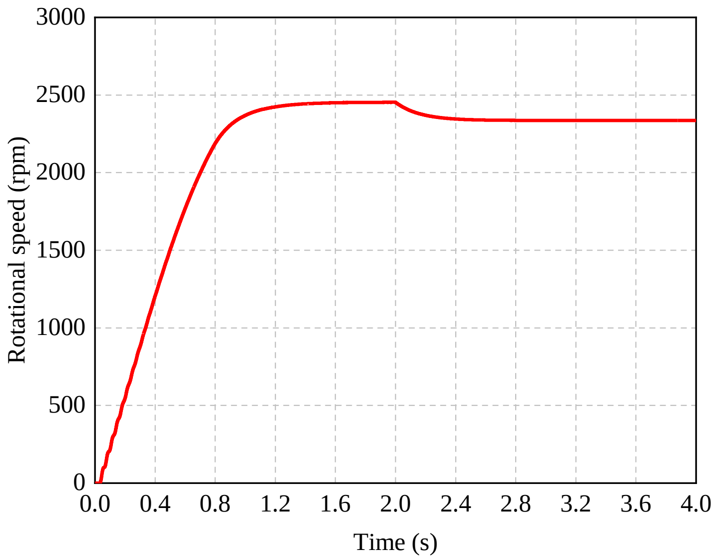

Fig. 16. Motor rotational speed response to an irradiance drop (G: 700→500 W/m^2)

As shown in Fig. 18, the pump only starts pumping water at a speed of 2154 rpm. It is also observed that there is a 0.8 s delay before the commencement of water flow from the pump. This period corresponds to the duration required for the pipeline filling before the circuit begins discharging water externally. Additionally, this period also corresponds to the time required for the total head to exceed the static head and dynamic head, see Fig. 17. It is noteworthy that in reality, the pump must overcome both the head losses, the dynamic head, and the static head of the hydraulic circuit to pump water. As can be seen from Fig. 19, a significant decrease in flow rate is observed during the decrease of irradiance, where it decreased from 0.775 l/s to 0.49 l/s. This is attributed to the decrease in generated power. The head losses are dependent on the flow rate, and their magnitude decreases as the flow rate decreases (Fig. 19).

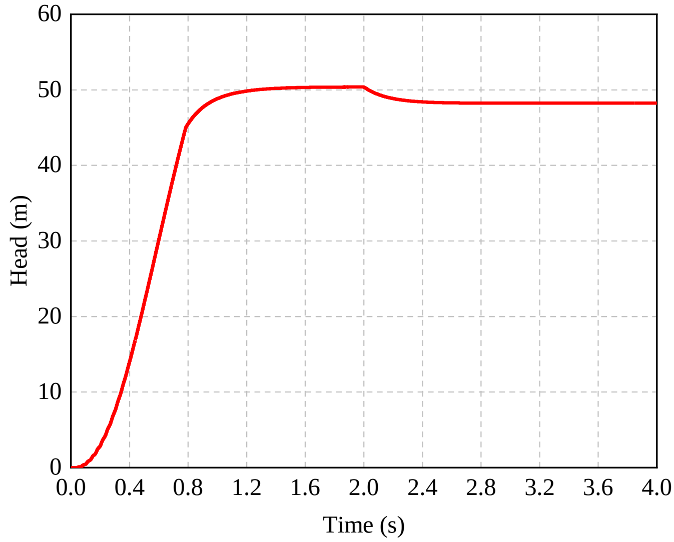

Fig. 17. Total pump head response to an irradiance drop (G: 700→500 W/m^2)

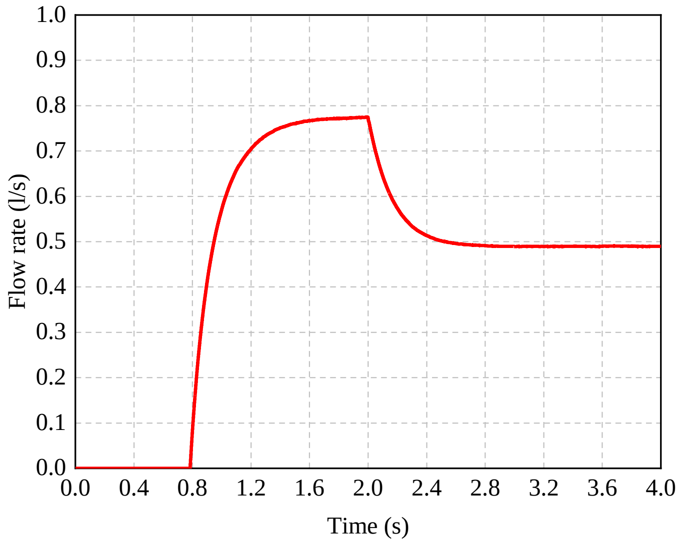

Fig. 18. Water flow rate response to an irradiance drop (G: 700→500 W/m^2)

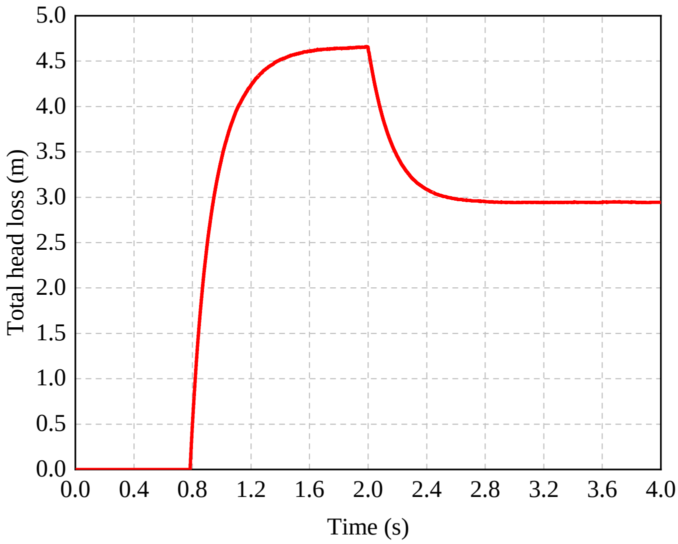

Fig. 19. Total head losses response to an irradiance step (G: 700→500 W/m^2)

4.1 Effect of Temperature

Subsequently, a step change in temperature from 25°C to 35°C was applied at t=2.0 s, while keeping irradiance constant at 600 W/m^2. The simulation results are depicted in Fig. 20 to Fig. 28, which represent, respectively, the variations over time of voltage and current at PV generator terminals, PV power, line voltages and line currents at the motor terminals, rotational speed, electromagnetic and load torques, total head, and water flow rate. From Fig. 20, a significant impact of temperature change on the PV voltage is observable, as it decreased from 405 V to 373 V; this is attributed to the notable influence of temperature levels on the Voc voltage. As depicted in Fig. 21, the temperature variations have a negligible impact on the PV current; this is attributed to the insignificant effect of temperature levels on the Isc current. According to Fig. 22, the increase in temperature leads to a notable reduction in the electrical power of the PV generator.

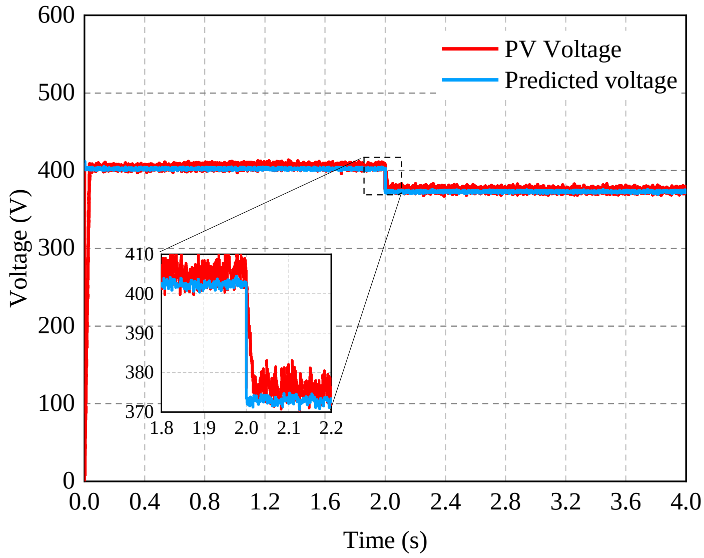

Fig. 20. PV voltage response to an increase in temperature (T: 25 → 35 °C)

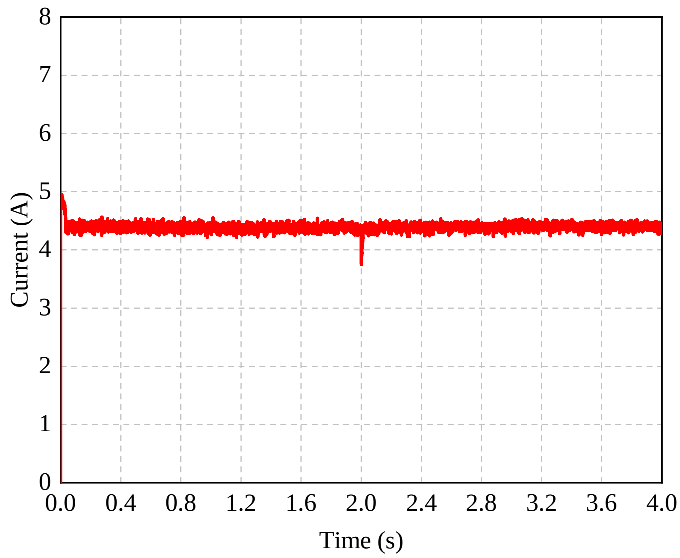

Fig. 21. PV current response to an increase in temperature (T: 25 → 35 °C)

From Fig. 23, it can be observed that the current demand did not change during the temperature variation. Conversely, the voltage at the motor terminals underwent a significant decrease, reaching 25 V during the temperature change (see Fig. 24). It is observed that upon reaching the steady state, the electromagnetic torque exhibits a fluctuation of approximately 0.25 Nm. This variation is attributed to the switching at the inverter and the requirements of the PMW regarding switching times. Based on Fig. 28, it is evident that the water flow rate increases to approximately

0.62 l/s when the system operates at 25 °C. Conversely, at 45 °C, there is a notable decrease in the flow rate.

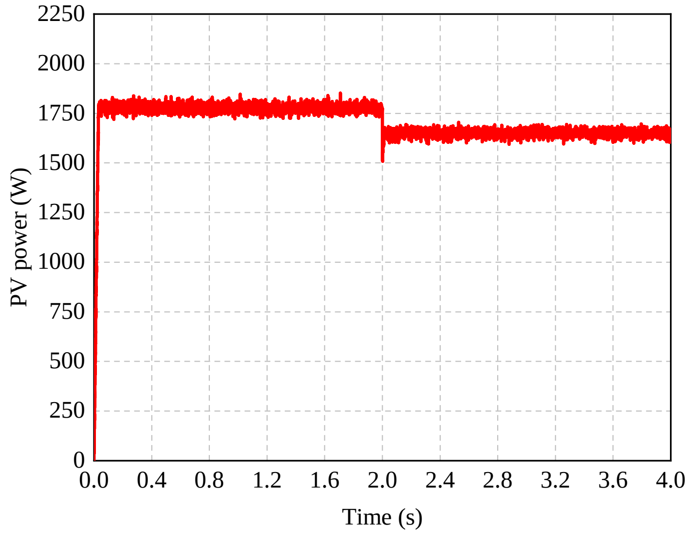

Fig. 22. PV power response to an increase in temperature (T: 25 → 35 °C)

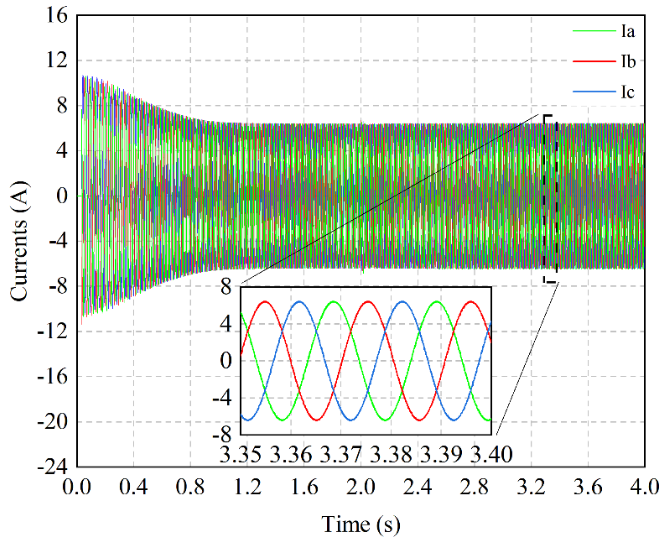

Fig. 23. Line current response to an increase in temperature (T: 25 → 35 °C)

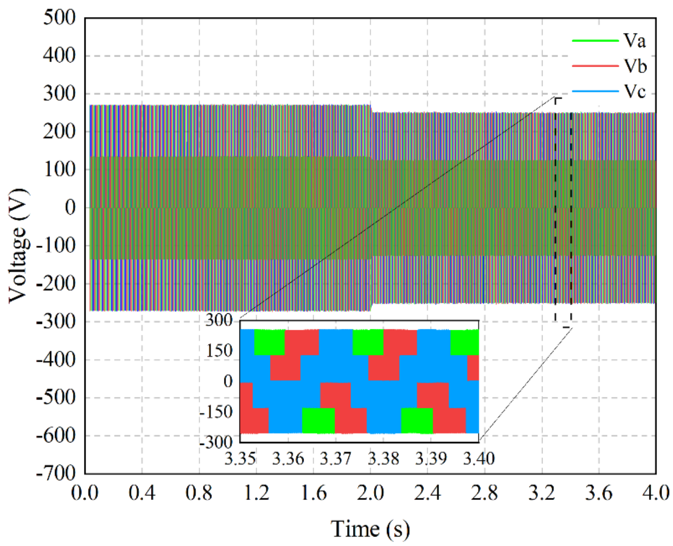

Fig. 24. Line voltages response to an increase in temperature (T: 25 → 35 °C)

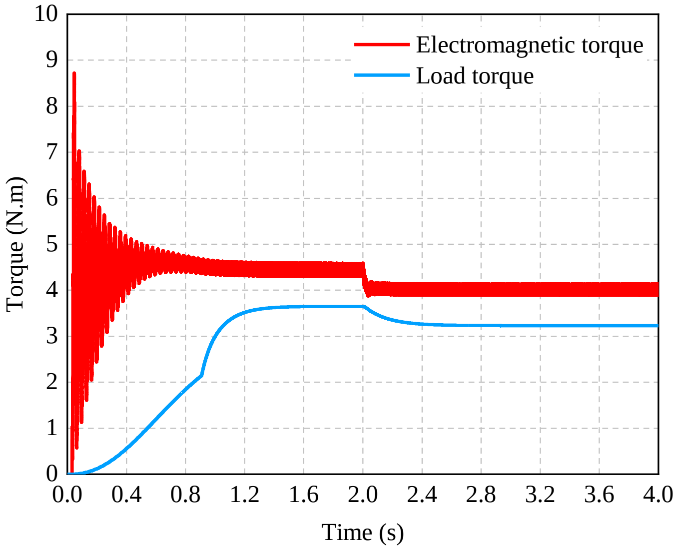

Fig. 25. Electromagnetic and load torque responses to an increase in temperature (T: 25 →35°C)

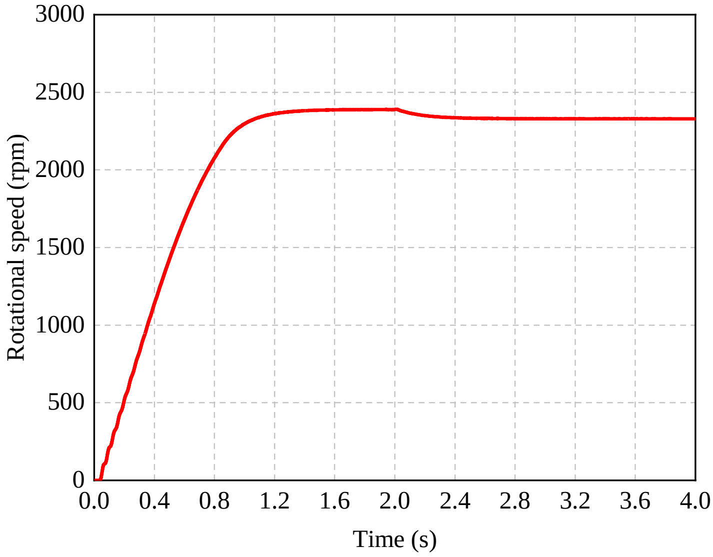

Fig. 26. Motor rotational speed response to an increase in temperature (T: 25 → 35 °C)

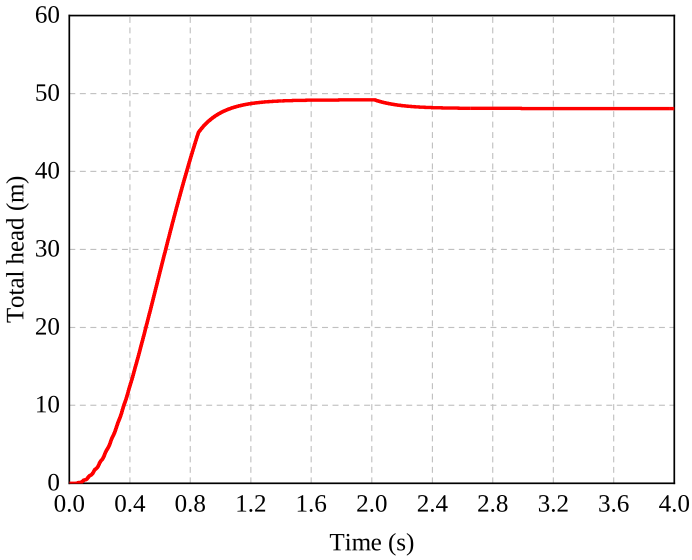

Fig. 27. Total pump head response to an increase in temperature (T: 25 → 35 °C)

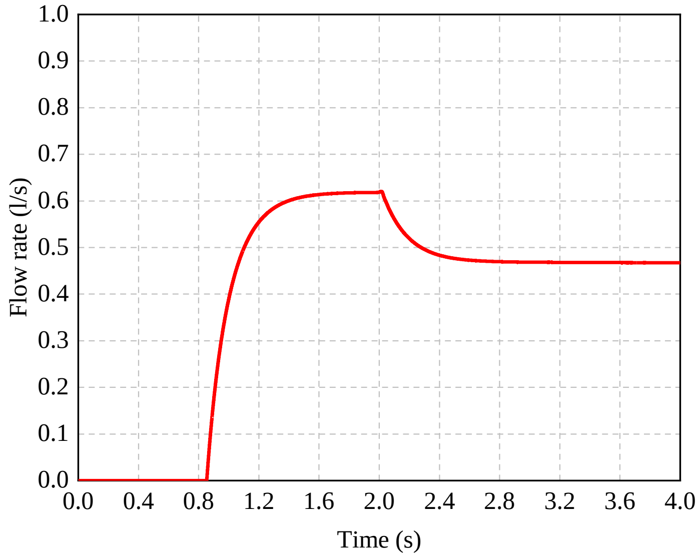

Fig. 28. Water flow rate response to an an increase in temperature (T: 25 → 35 °C)

5. Conclusions

This paper presents a dynamic simulation for a PVWPS to analyze its performance under varying irradiance and ambient temperature. The major conclusions are as follows:

- The parameters of the target PV module KC200GT were identified using three methods: Newton–Raphson, fsolve, and particle swarm optimization (PSO). In terms of identification accuracy, PSO shows excellent agreement between the simulated I–V curve and the manufacturer's data, with a higher R^2 of 0.9901 and a lower RMSE of 0.0358. The identified parameters are then used to accurately reproduce the behavior of the target PV module within the dynamic simulation.
- The manufacturer's data for the centrifugal pump, usually provided for a single nominal speed, were used to develop a pump model capable of predicting the flow rate, head, and load torque at different rotational speeds.
- Four machine-learning models (ANN, ANFIS, SVM, and GPR) were developed and compared to predict the MPP voltage of the PV generator. Based on this comparative study, ANFIS stands out due to its high predictive accuracy, outperforming the other models and conventional MPPT methods. Furthermore, the ANFIS model was combined with a PI controller to ensure MPP tracking, which effectively maintains the PV voltage close to the optimal value with a fast response time of 0.04 s.
- To assess the effectiveness and robustness of the PVWPS control strategy, sudden changes in irradiance and ambient temperature were applied. While variations in irradiance have a negligible effect on the optimal MPP voltage, a sudden drop in irradiance significantly reduces the PV current and power, leading to a noticeable decrease in water flow rate. An increase in ambient temperature causes a marked reduction in PV-generated power due to the drop in PV voltage. In contrast, the PV current remains almost unchanged, which also results in a lower water flow rate. These results confirm the direct coupling between PV power and the hydraulic performance of the pumping system.

Appendix A

A.1 ANN Approach

A standard feedforward artificial neural network (ANN) was employed. Its architecture consists of input, hidden, and output layers. The hidden layer contains neurons that perform internal processing. The neuron's output (s_j) is calculated as follows:

$$s_j = g\left(\sum_{i=1}^{m} w_{ij} \cdot e_i - b_j\right) \tag{A.1}$$

The weights (wij) and bias (bj) are adjustable parameters. Users can select the transfer function, number of hidden layers and neurons, and training algorithm to optimize performance. A linear transfer function was chosen for the output, and a hyperbolic tangent sigmoid one for the hidden layer to obtain better performances. The used training function is the Bayesian Regularization. After the training phase for different numbers of hidden neurons, the best configuration is given for a 2-3-1 structure.

A.2 ANFIS

The ANFIS architecture is characterized by five layers. For an ANFIS configured with two inputs, denoted as x1 and x2, the output of each layer is determined by the following equations:

$$L_{1,i} = \mu A_i(x_1),\ \ for\ \ i = 1,2 \ldots j \tag{A.2}$$

$$L_{1,i} = \mu B_i(x_2), fori = 1,2 \ldots j \tag{A.3}$$

$$L_{2,i} = W_i = \mu A_i(x_1) \cdot \mu B_i(x_2), fori = 1,2 \ldots j^2 \tag{A.4}$$

$$L_{3,i} = \bar{W}_i = \frac{W_i}{\sum_{i=1}^{j^2} W_i} \tag{A.5}$$

$$L_{4,i} = \bar{W}_i f_i = \bar{W}_i(p_i x_1 + q_i x_2 + r_i) \tag{A.6}$$

$$L_{5,i} = \sum_{i=1}^{j^2} \bar{W}_i f_i = \frac{\sum_{i=1}^{j^2} W_i f_i}{\sum_{i=1}^{j^2} W_i} \tag{A.7}$$

where, (μAi, μBi): Membership functions, (p_i, q_i, r_i): Linear parameters.

A.3 GPR model

Given a training dataset of input (x_i) and target (y_i) values, the relationship between them can be modeled as follows:

$$y_i = f(x_i) + \zeta_i \tag{A.8}$$

The model includes additive Gaussian noise with a mean of zero and variance. In a distributed Gaussian process, f(xi) can also be represented as:

$$f(x_i) \approx GP(m(x_i), K(XX'')) \tag{A.9}$$

where, K(X, X'): Covariance matrix, $m(x_i) = E[f(x_i)]$: Expectation function for input x_i.

A.4 SVM model

The learned parameters of the SVM regression model comprising support vectors, coefficients, and bias term are extracted to formulate the predictive regression function done by:

$$f(x) = \sum_{i=1}^{n} \alpha_i K(X_i, x) + b \tag{A.10}$$

For the present study, the SVM model was trained by an RBF kernel function given by:

$$K(x_i, x_j) = G(x_i, x_j) = exp\left(-\frac{\|x_i - x_j\|^2}{2\sigma^2}\right) \tag{A.11}$$

where, σ2: Variance.

Appendix B

Table B. System Parameters

Element	Parameter	Value
PV Generator (STC)	Module type	KC200GT
	Maximum power	200 W
	Voltage at MPP	26.3 V
	Current at MPP	7.61 A
	Short circuit current	8.21 A
	Open circuit voltage	32.9 V
	Temperature coefficient of Isc	3.18×10^{-3} A/°C
	Number of cells	54 per module
	Module's configuration	14 in series
Squirrel cage motor	Nominal power	2200 W
	Nominal speed	2900 rpm
	Nominal line-to-line voltage	380 V
	Nominal frequency	50 Hz
	Stator winding resistance	6.18 Ω
	Stator inductance	0.688 H
	Mutual inductance	0.678 H
	Rotor winding resistance	4.38 Ω
	Rotor inductance	0.688 H
	Pole pair	1
	Rotor inertia moment	0.012 $kg \cdot m^2$
	Viscous torque constant	0.0033 N·m·s
Hydraulic circuit	Static head	45 m
	Length of pipe	47 m
	Inside pipe diameter	0.04 m
	Pipe wall roughness	0.15 mm
	Computed friction factor	0.0502
	Total fitting loss coefficient	13.5
	Specific drawdown	-1.67 $m/(m^3/h)$

Appendix C

Table C. Manufacturer Data of Centrifugal Pump (Bombas Ideal VIP 9/6) for Nn = 2900 rpm

Q (l/s)	H (m)	η (%)	Computed T_r (N·m)
0.83522	74.14586	45.24	4.42235
1.11089	71.82246	50.61	5.09244
1.38758	68.57708	55.09	5.58015
1.67142	65.36857	58.39	6.04412
1.94709	61.23808	59.56	6.46701
2.22378	55.37426	59.56	6.67876
2.49945	48.33031	57.49	6.78744
2.77614	41.32323	53.88	6.87756
3.05181	33.98424	48.51	6.90689

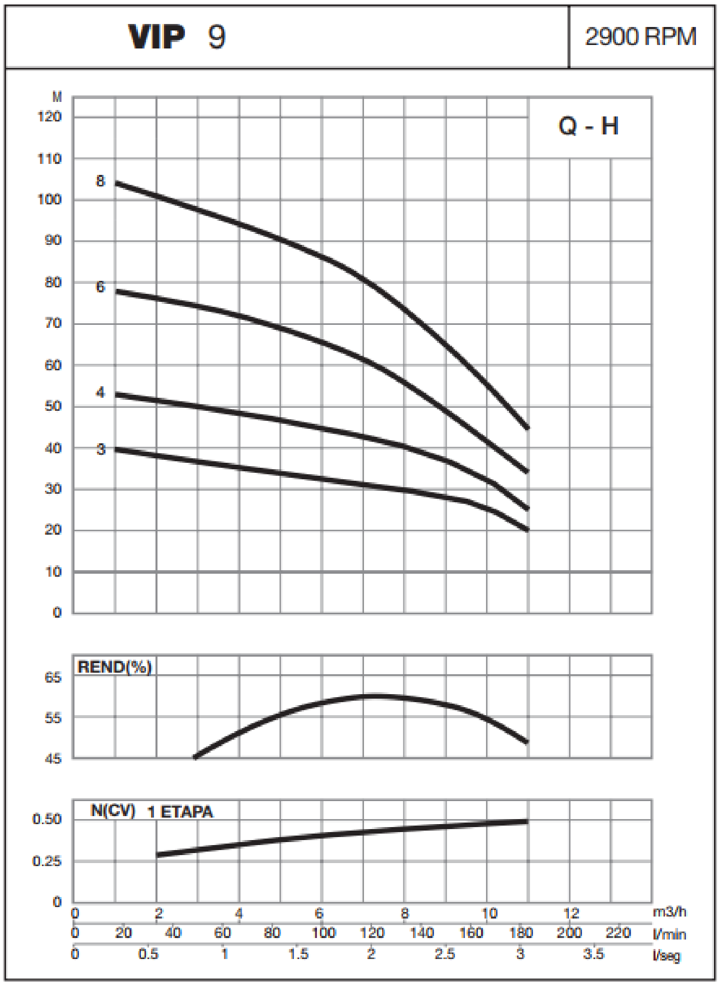

Fig. C. The efficiency curve of the pump (Bombas Ideal VIP 9/6)

References

[1] Haddad S, Benghanem M, Mellit A, Daffallah KO. ANNs-based modeling and prediction of hourly flow rate of a photovoltaic water pumping system: experimental validation. Renewable and Sustainable Energy Reviews, 2015; 43:635-643. https://doi.org/10.1016/j.rser.2014.11.083

[2] De Leone R, Pietrini M, Giovannelli A. Photovoltaic energy production forecast using support vector regression. Neural Computing and Applications, 2015; 26(8):1955-1962. https://doi.org/10.1007/s00521-015-1842-y

[3] Nageem R, R J. Predicting the power output of a grid-connected solar panel using multi-input support vector regression. Procedia Computer Science, 2017; 115:723-730. https://doi.org/10.1016/j.procs.2017.09.143

[4] Mahesh PV, Meyyappan S, Alla R. Support vector regression machine learning based maximum power point tracking for solar photovoltaic systems. International Journal of Electrical and Computer Engineering Systems, 2023; 14(1):100-108. https://doi.org/10.32985/ijeces.14.1.11

[5] Chandra S, Gaur P, Pathak D. Radial basis function neural network based maximum power point tracking for photovoltaic brushless DC motor connected water pumping system. Computers and Electrical Engineering, 2020; 86:106730. https://doi.org/10.1016/j.compeleceng.2020.106730

[6] El Haji I, Megrini M, Kchikach M, Sahbani S, Gaga A, El Hasnaoui A. Performance optimization of symmetrical multi-level boost converter using hybrid MPPT-ANN for solar energy applications. Results in Engineering; 2025; 26:104729. https://doi.org/10.1016/j.rineng.2025.104729

[7] Sharkawy A-N. The effect of increasing hidden layers on the performance of the deep neural network: Modelling, investigation, and evaluation. Res. Eng. Struct. Mater., 2025; 11(4): 1633-1651. http://dx.doi.org/10.17515/resm2024.442st0909tn

[8] Alice Hepzibah A, Premkumar K. ANFIS current-voltage controlled MPPT algorithm for solar powered brushless DC motor based water pump. Electrical Engineering, 2019; 102(1):1-11. https://doi.org/10.1007/s00202-019-00885-8

[9] Sarkar R, Kumar JR, Sridhar R, Vidyasagar S. A new hybrid BAT-ANFIS-based power tracking technique for partial shaded photovoltaic systems. International Journal of Fuzzy Systems, 2021; 23(5):1313-1325. https://doi.org/10.1007/s40815-020-01037-y

[10] Pachaivannan N, Subburam R, Padmanaban M, Subramanian A. Certain investigations of ANFIS assisted CPHO algorithm tuned MPPT controller for PV arrays under partial shading conditions. Journal of Ambient Intelligence and Humanized Computing, 2021; 12(10):9923-9938. https://doi.org/10.1007/s12652-020-02738-w

[11] Ahmed MM, Hassanien WS, Enany MA. Modeling and evaluation of SC MPPT controllers for PVWPS based on DC motor. Energy Reports, 2021; 7:6044-6053. https://doi.org/10.1016/j.egyr.2021.09.055

[12] Hilali A, El Ouanjli N, Mahfoud S, Al-Sumaiti AS, Mossa MA. Optimization of a solar water pumping system in varying weather conditions by a new hybrid method based on fuzzy logic and incremental conductance. Energies, 2022; 15(22):8518. https://doi.org/10.3390/en15228518

[13] Boussafa A, Rabeh R, Ferfra M, Chennoufi K. Experimental test of optimizing maximum power point tracking performance in solar photovoltaic arrays based on backstepping control and optimized by genetic algorithm. Results in Engineering, 2024; 23:102746. https://doi.org/10.1016/j.rineng.2024.102746

[14] Juarez-Perez EJ, Momblona C, Casas R, Haro M. Enhanced power-point tracking for high-hysteresis perovskite solar cells with a galvanostatic approach. Cell Reports Physical Science. 2024; 5(4):101213. https://doi.org/10.1016/j.xcrp.2024.101885

[15] Chen B. High frequency design and efficiency optimization of LLC resonant converter based on SiC devices. Applied and Computational Engineering, 2025; 145:176-181. https://doi.org/10.54254/2755-2721/2025.22243

[16] Chandel SS, Nagaraju Naik M, Chandel R. Review of solar photovoltaic water pumping system technology for irrigation and community drinking water supplies. Renewable and Sustainable Energy Reviews, 2015; 49:1084-1099. https://doi.org/10.1016/j.rser.2015.04.083

[17] Santbergen R, van Zolingen RJC. The absorption factor of crystalline silicon PV cells: a numerical and experimental study. Solar Energy Materials and Solar Cells, 2008; 92(4):432-444. https://doi.org/10.1016/j.solmat.2007.10.005

[18] Belarbi M. Modeling and simulation of a PV pumping system. Magister, University of Sciences and Technology - Oran, Algeria, 2006.

[19] Bose BK. Power electronics and motor drives: advances and trends. Amsterdam: Elsevier Academic Press, 2006. https://doi.org/10.1109/CIEP.2006.312138

[20] Nassar-Eddine I, Obbadi A, Errami Y, El Fajri A, Agunaou M. Parameter estimation of photovoltaic modules using iterative method and the Lambert W function: a comparative study. Energy Conversion and Management, 2016; 119:37-48. https://doi.org/10.1016/j.enconman.2016.04.030

[21] Benahmida A, Maouhoub N, Tifidat K, Sahsah H. Extraction of photovoltaic generator parameters through combination of an analytical and iterative approach. International Journal of Electrical and Computer Engineering, 2022; 12(5):4529-4537. https://doi.org/10.11591/ijece.v12i5.pp4529-4537